Channel Measurements and Modeling for Low-Terahertz Band Vehicular Communications

Johannes M. Eckhardt, Vitaly Petrov, *Member, IEEE*, Dmitri Moltchanov, Yevgeni Koucheryavy, *Senior Member, IEEE*, and Thomas Kürner, *Fellow, IEEE*

***Abstract*— Wireless communications in the low terahertz band (0.1 THz–1 THz) is a promising candidate to enable ultra-high-rate vehicular networks beyond 5G. The successful design and adoption of such systems require a deep understanding of the low THz channel specifics in complex vehicular scenarios. In this paper, a comprehensive measurement campaign is reported with the aim of analyzing the wave propagation at 300 GHz in typical vehicular deployments. Following a modular approach, the generic vehicular scenario is decomposed into basic propagation setups that are further analyzed in detail. The obtained measurement data are then applied to derive the mathematical approximations that characterize the low THz band channel properties for each scenario. Finally, the combination of measurement and modeling results is used to identify the critical propagation effects that has to be accounted for in the applied studies. The presented approach, raw and processed data, as well as the contributed analysis, serve as building blocks for future analytical and simulation tools to model prospective vehicular communication systems in the low THz band.**

***Index Terms*— THz, vehicular communications, channel measurements, propagation models, beyond 5G.**

I. Introduction

TODAY, as the first standardization wave of fifth-generation (5G) millimeter wave communications systems is almost complete, the terahertz band (0.1 THz – 10 THz) starts to receive attention from the academic and industrial communities. Particularly, the region between 0.1 THz and 1 THz, often referred to as *low THz band*, is considered as a potential frequency range for beyond-5G and 6G wireless networks [1]–[3]. Identified as the next frontier for wireless access systems, this band promises significant improvements in the data rates and the densities of the connected devices [4]. To this aim, the use of highly-directional THz systems allows not only to reach sufficient communication range [5], but also to reduces the impact of interference between the nodes [6].

Manuscript received July 7, 2020; revised February 11, 2021; accepted March 1, 2021. Date of publication April 13, 2021; date of current version May 18, 2021. *(Corresponding author: Johannes M. Eckhardt.)*

Johannes M. Eckhardt and Thomas Kürner are with the Institut für Nachrichtentechnik, Technische Universität Braunschweig, 38106 Braunschweig, Germany (e-mail: eckhardt@ifn.ing.tu-bs.de; kuerner@ifn.ing.tu-bs.de).

Vitaly Petrov was with the Unit of Electrical Engineering, Tampere University, 33100 Tampere, Finland. He is now with Nokia Bell Labs, 02610 Espoo, Finland (e-mail: vitaly.petrov@nokia.com).

Dmitri Moltchanov and Yevgeni Koucheryavy are with the Unit of Electrical Engineering, Tampere University, 33100 Tampere, Finland (e-mail: dmitri.moltchanov@tuni.fi; evgeny.kucheryavy@tuni.fi).

Color versions of one or more figures in this article are available at https://doi.org/10.1109/JSAC.2021.3071843.

Digital Object Identifier 10.1109/JSAC.2021.3071843

Following the recent advances in the design of *fixed* low THz band links for wireless backhauling and wireless augmented data centers [7], [8], vehicular communications is considered as one of the attractive usage scenarios for *mobile* low THz networks [9], [10]. Particularly, high-rate directional low THz links may be used to exchange the massive amounts of data generated by the future fleets of (semi)autonomous vehicles performing collective driving [11]. Further, the THz vehicular links may also facilitate data relaying, thus offloading traffic from congested cellular networks [12]. As per existing spectrum regulations, the prospective low-THz systems are expected to notably outperform the state-of-the-art mmWave solutions in rate-oriented scenarios, as they offer much wider channel bandwidth [2]. Particularly, the recently released IEEE Std. 802.15.3d–2017 for low-THz connectivity already considers channels of up to 69 GHz, which is an order of magnitude greater than existing 2.16 GHz -wide channels for modern IEEE and 3GPP solutions at 60 GHz [13].

Vehicular communication systems in the low THz band are less limited by the battery-, power-, and size-related constraints than regular handheld and wearable devices, which facilitates their early adoption [10]. At the same time, the successful utilization of low THz band vehicular communications calls for an in-depth study on the propagation at these frequencies in vehicular deployments. Here, real measurement data can be used as reference facilitating the development and calibration of scenario-specific channel and interference models for low THz band vehicular communications.

Some measurements on low THz propagation in different environments have been performed in previous studies. The authors in [14] compared the characteristics of mmWave and low THz intra-device communications, particularly highlighting the difference in signal propagation at 60 GHz and 300 GHz. Reference measurements for indoor low THz connectivity were reported in [15], where the authors also confirm that the shape and the material of the obstacles present in the environment notably affect the characteristics of the low THz propagation. The main features of low THz communications in the data center were identified and analyzed in [16], while the outdoor measurements for the wireless links above 100 GHz were presented in [17]. Finally, the details of train-to-infrastructure low THz communications were revealed in [18].

The presented studies illustrate that the propagation characteristics of low THz links may differ substantially depending on the environment of interest. This observation motivates further investigations on the characteristics of low THz signal propagation in vehicular communication deployments.

The previous measurement studies in the field of vehicular communications primarily focused on lower frequencies, such as 36 GHz in [19], 60 GHz in [20] and [21], 77 GHz in [22], among others. Later, the characteristics of the materials in vehicular deployments (such as glass, metal, and plastic) were explored in [23]. Finally, a preliminary study on penetration and reflection losses at 300 GHz in vehicular scenarios were reported in [24], but for a limited set of scenarios and without any detailed analysis or modeling.

Summarizing, no throughout measurement campaign for low THz signal propagation in vehicular setups has been reported to date challenging the design of trustworthy channel and interference models for prospective vehicular communication systems. We aim to address this gap in the present article.

The main contributions of our study are:

- To support the design of low THz vehicular channel and interference models, we *perform a comprehensive measurement campaign*, characterizing the channel impulse response (IR), average path loss, and other important angular and time-dependent characteristics in various single-lane and multi-lane deployment scenarios. We also compare the results with the corresponding data available for mmWave vehicular systems, where applicable.
- To facilitate the understanding of low THz signal propagation in vehicular scenarios, we analyze the obtained measurement results and *identify the main components affecting the channel of low THz vehicular communication systems in different conditions*. For complex dependencies, simpler approximations are proposed and compared with the measurement data. The obtained results and contributed models can be further utilized in link-level and system-level modeling of prospective low THz vehicular communication systems.

The rest of the paper is organized as follows. The measurement equipment and the associated methodology for calibration and data processing are described in Section II. The measurement setups and the obtained results for the single-lane vehicular scenarios are detailed in Section III. Further, Section IV introduces the measurement setups and the selected results for the multi-lane vehicular scenarios. The main findings and the general conclusions are summarized in Section V.

II. Measurement Methodology

This section is dedicated to the methodology of the performed channel measurements. We first introduce the considered scenarios and the two categories of the performed measurements in Subsection II-A. We then describe the measurement equipment in Subsection II-B. Finally, we detail the data post-processing and calibration procedures in Subsection II-C.

A. Measurement Environment and Setups

The measurement campaign was conducted in the Lower Saxony Automotive Research Center (NFF), Braunschweig, Germany. In order to facilitate the long-term measurement campaign and also to reduce the influence of the atmospheric effects on the accuracy of the results, a dedicated trial field inside the NFF premises with a dimensions of approximately 25 m $\times$ 15 m has been allocated for the measurements. The allocated area has been configured to model a segment of a road with two lanes in each direction. We use the standard lane width of 3.60 m. The floor is made of concrete, making the results representative for the typical concrete-based road surfaces [25] and a first-order approximation for other types of road surfaces (i.e., asphalt) [22]. The data and models reported in this article may also serve as baseline for further detailed investigations of the impact of the road shape, as well as surface material, composition, and conditions (i.e., wet or dry and hot or cold road pavement) that demand a separate dedicated study [26].

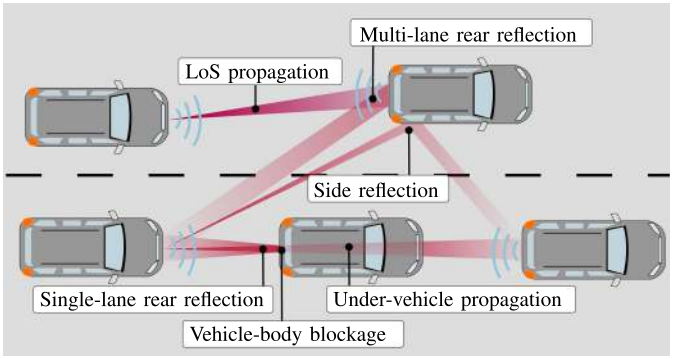

Fig. 1. Typical scenario for low THz band vehicular communications with complex propagation effects.

The chosen set of measurement setups is intended to model the typical configurations for prospective directional vehicular communications, where low THz signals may penetrate through, as well as be reflected, scattered, and diffracted from the vehicle body. As observed in Fig. 1, the low THz signal propagation in the vehicular environment is complex and may be affected by multiple vehicles. In order to obtain the measurement results and analyze the impact of individual components, we first decompose the realistic setup into a number of simpler scenarios that can be studied separately.

In each scenario, there are three parties involved: (i) the transmitter (TX) device that represents the vehicle currently transmitting the low THz signal; (ii) the receiver (RX) device that represents the vehicle currently receiving the low THz signal; and the vehicle under test (VUT) that is a real vehicle having an impact on the propagation channel in the dedicated setup. The VUT is a typical sport utility vehicle (SUV), particularly, the Volkswagen Tiguan II (model 2018) with the length of 4486 mm, the width of 1839 mm and the height of 1657 mm. Our general setup is illustrated in Fig. 2.

Two main groups of measurements have been performed during the campaign:

- *Single-lane measurements.* The first group of measurements studies the setups, where *all the involved vehicles stay in the same lane*. For these setups, both TX and RX are mounted on tripods that allow for exploring the propagation effects for different separation distances between the modeled vehicles, as well as for different

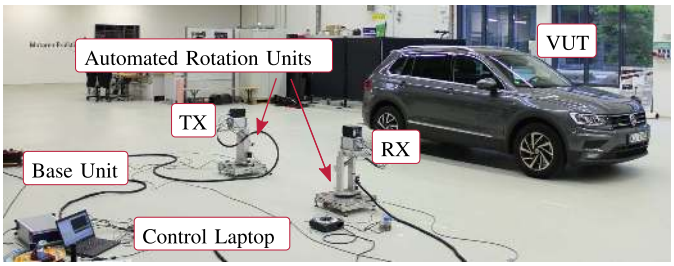

Fig. 2. Illustration of the general measurement setup.

heights of the TX and the RX. The setups, collected data, and main observations for the single-lane measurements are further detailed in Section III.

- *Multi-lane measurements.* The second group of measurements studies the setups, where the involved parties are located on several lanes. Here, the propagation of the directional low THz signal is also subject to the current pointing directions of the TX and RX antenna systems. To capture this additional dependency, the custom-made automated rotation units are used that enable a programmable sweep of a definable angular range of the horizontal plane with a selectable step size. The rotation units are integrated and controlled in the Matlab channel sounder interface. Hence, the temporal analysis of the IR can be enlarged with a spatial analysis where the angle of depature (AoD) and angle of arrival (AoA) of the various multi path component (MPC) are investigated. The setups, collected data, and main observations for the multi-lane measurements are further detailed in Section IV.

It is important to emphasize that we do not classify the measurement setups in channel measurements and interference measurements (what might be intuitive and known from prior campaigns in cellular network environment). The reason is that the investigated channel may be treated as the useful signal or the interference depending on the use case.

B. Measurement Equipment

The measurement data was obtained with the low THz band channel sounder manufactured by Ilmsens that is able to connect up to four TXs and RXs simultaneously [27]. The channel sounder is composed of a base unit, a control laptop, a TX and an RX (see Fig. 3).

The base unit creates the common clock signal of 9.22 GHz that is distributed to all ultra-wide band (UWB) modules. The pseudo random noise generator (PNG) of the TX module creates a pseudo-random M-sequence of order 12 that is converted to the low THz range from 300.2 GHz to 308.2 GHz by the frequency extender and transmitted with the transmit power of -23.7 dBm. The signal is radiated and received by identical horn antennas with a gain of 26.4 dBi and a half-power beam width (HPBW) of 8.5°.

At the RX the received signal is downconverted to the baseband. The common clock signal, which is first frequency-doubled to 36.22 GHz, then to 147.52 GHz and amplified, serves as local oscillator for mixing the received

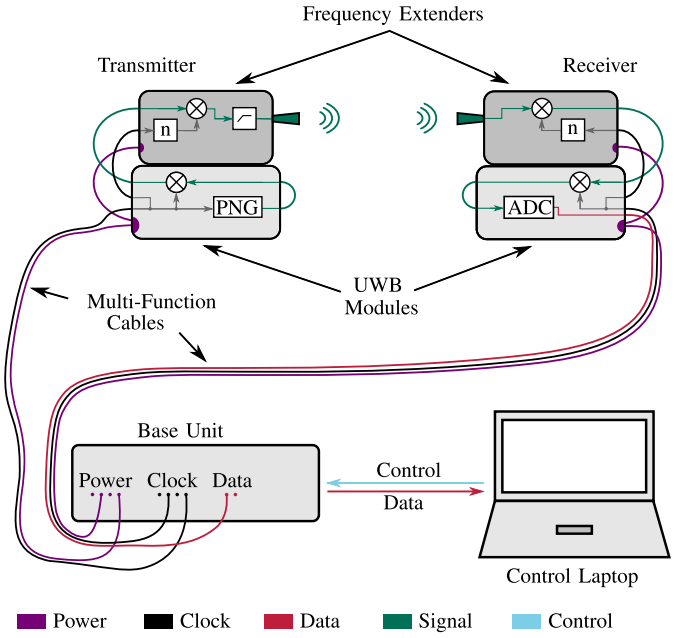

Fig. 3. Schematic view of the employed channel sounder.

signal in a sub-harmonic mixer. After that, the in-phase and quadrature signals are sampled with two analog-to-digital converters (ADCs) using a subsampling factor of 128. Thus, the measurement rate yields to 17590 IR/s and the maximum measurable delay results to 444.14 ns. Finally, the channel sounder processes the cross-correlation of the transmitted and received signals to obtain the relative IR which is then calibrated with a calibration factor as detailed in the following subsection. More information on the sounder is available in [27].

C. Calibration and Postprocessing

Every time the channel sounder is switched on, a calibration measurement in a back-to-back setup is performed. This calibration accounts for the arbitrary delay introduced in the PNG, the subsampling mechanism, and the varying power levels of the different UWB modules. The antennas are replaced by waveguides with a known attenuation and delay to eliminate the influence of the channel. The IR of the back-to-back measurements is compared to the known waveguide attenuation to calculate the calibration factor in terms of power and delay.

The directional horn antenna acts as a spatial filter and allows to resolve the various MPCs in space. In order to reduce the influence of the antenna pattern, the polarization is chosen in such a way that the H plane having a lower side lobe level lies in the plane of interest. This results in a vertical polarization for rotational measurements and a horizontal polarization for tripod-based measurements.

Since the measurements are performed in a static scenario, the channel sounder can increase its dynamic range to 60 dB by averaging multiple IRs. In our campaign, 64 IRs are averaged on a hardware level to reduce the amount of data that is transferred to the control laptop. Besides, the software

is configured to average over 2048 IRs for the rotational measurements and over 16384 IRs for the tripod-based measurements resulting in 131072 and 1048576 overall measured IRs for every configuration, respectively. The average settings represent a trade-off between precision and measurement speed and are determined in an empirical way. The spurious free dynamic range remains constant at 20 dB independent of the averaging. However, since the spurious peaks originating from the sounder system are linked to the received power it limits the dynamic range only if a strong component is present within the small receiving angle of the antenna. It is noteworthy that the bending of the multi-function cables during the rotation of the units has an influence on the clock on the order of picoseconds and thus does not affect the measurement in a significant way.

The further postprocessing of the measured IRs includes an interpolation and a cut of the IR at the maximum delay of interest in order to eliminate the influence of the environment. To combine the spatially resolved IRs to one IR of the channel that would have been measured with omni-directional antennas the omni-directional IR (ODIR) is calculated according to

$$|h_{\text{ODIR}}(\tau)|^2 = \sum_{k=1}^{K} |h_k(\tau_{\max})|^2 \, \delta(\tau - \tau_{\max}) + \sum_{n=1}^{N} |\epsilon_{\text{Re}} + \mathrm{j}\, \epsilon_{\text{Im}}|^2 \, \delta(\tau - \tau_n) \,, \quad (1)$$

where $h_k(\cdot)$ denotes the IR of the kth combination of AoD and AoA, $\delta(\cdot)$ denotes the Dirac delta function, τ denotes the delay, $\tau_{\max}$ denotes the delay of the maximum peak of the IR, ϵ_{Re} and ϵ_{Im} denote two Gaussian random variables that create a synthetic noise with the same variance as the noise of the spatially resolved measurements, and τ_n the delay of the nth sample, respectively. Further, N provides the number of samples of the IR and K the number of combinations of AoDs and AoAs, respectively [28].

To quantify the impact of the MPCs two important quantities are utilized. The root mean square delay spread (RMSDS) given by

$$\tau_{\text{DS}} = \sqrt{\frac{\sum_{n=1}^{N} \tau_n^2 \cdot |h(\tau_n)|^2}{\sum_{n=1}^{N} |h(\tau_n)|^2} - \left(\frac{\sum_{n=1}^{N} \tau_n \cdot |h(\tau_n)|^2}{\sum_{n=1}^{N} |h(\tau_n)|^2} \right)^2} \quad (2)$$

acts as a variance of the MPC distribution in time. The angular spread represents the counterpart in the spatial domain. Here, the angular spread of departure (ASoD) and the angular spread of arrival (ASoA) are defined as

$$\theta_{\text{AS,AoX}} = \sqrt{\frac{\sum_{x=1}^{X} \phi_x^2 P_{\text{AoX}}(\phi_x)}{\sum_{x=1}^{X} P_{\text{AoX}}(\phi_x)} - \left(\frac{\sum_{x=1}^{X} \phi_x P_{\text{AoX}}(\phi_x)}{\sum_{x=1}^{X} P_{\text{AoX}}(\phi_x)} \right)^2} \quad (3)$$

with $P_{\text{AoX}}(\phi_x)$ replaced by

$$P_{\text{AoD}}(\phi_i) = \frac{1}{N} \sum_{n=1}^{N} \sum_{j=1}^{J} |h(\tau_n, \phi_i, \phi_j)|^2 \quad (4)$$

(a) Measurement setup

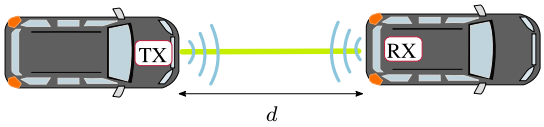

(b) Schematic view

Fig. 4. Setup for the LoS propagation.

for the AoD and by

$$P_{\text{AoA}}(\phi_j) = \frac{1}{N} \sum_{n=1}^{N} \sum_{i=1}^{I} |h(\tau_n, \phi_i, \phi_j)|^2 \quad (5)$$

for the AoA, respectively. Here, ϕ_i denotes the AoD and ϕ_j the AoA, I and J the number of rotation steps of the TX and the RX, respectively.

The resulting IRs are finally processed to obtain the average path loss, the RMSDS, the power angular profile (PAP) and the angular spreads. We now proceed describing the measurement setups and the selected results for the single-lane scenarios in the following section.

III. Single-Lane Measurements and Modeling

In this section, we report and analyze our measurements in a single-lane vehicular communications environment. We first discuss the line-of-sight (LoS) propagation in Subsection III-A. We then study the effect of vehicle-body blockage in Subsection III-B. Later, we explore the feasibility of the low THz signal propagation under the vehicle in Subsection III-C. We finally evaluate the low THz signal losses when reflecting from the front and rear sides of the vehicle in Subsection III-D.

A. Line-of-Sight Propagation

The measurement setup representing the case of unobstructed LoS communications is shown in Fig. 4. These measurements are performed in LoS propagation conditions for different heights of TX and RX, h, and different separation distances between the TX and the RX, d. Out of all the considered heights we specifically emphasize the importance of the following: (i) bumper level, $h = 0.4$ m, (ii) hood level, $h = 0.78$ m and (iii) windshield level, $h = 1.3$ m . These heights suit well as potential locations of TX and RX antenna systems for low THz vehicular communications.

The measurement results for this setup are illustrated in Fig. 5. This figure presents the total path loss of the low THz vehicular link as a function of the separation distance between

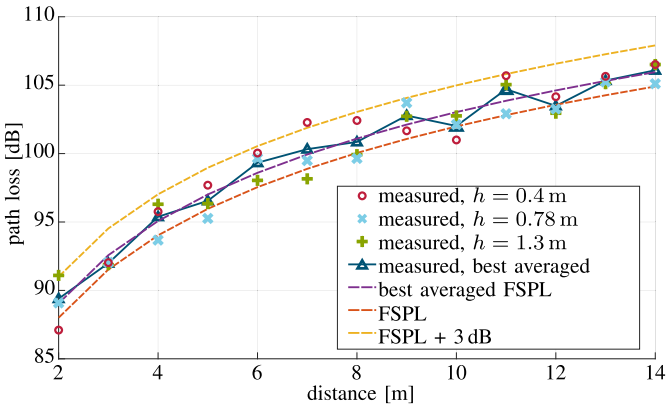

Fig. 5. Measured and modeled path loss for LoS conditions.

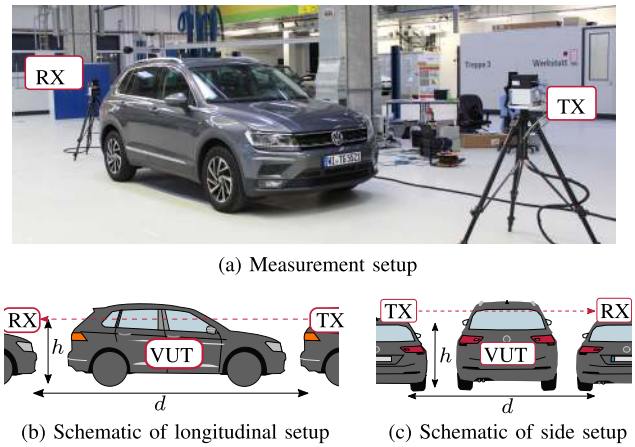

(a) Measurement setup

(b) Schematic of longitudinal setup

(c) Schematic of side setup

Fig. 6. Setup for the vehicle-body blockage.

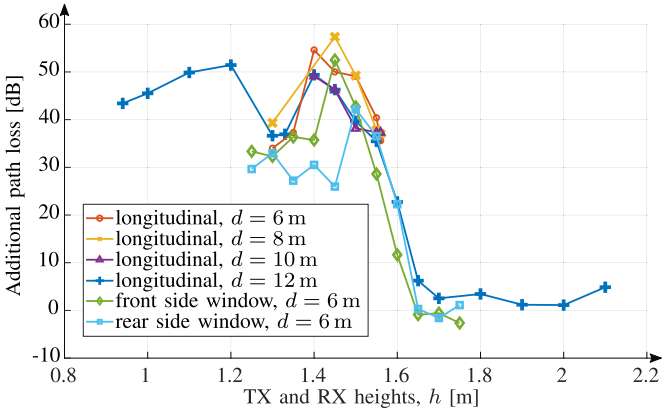

Fig. 7. Measured path loss for vehicle-body blockage.

the TX and the RX nodes. Analyzing the presented data, one may observe that the increase in the distance between TX and RX expectedly leads to higher path loss. Furthermore, the measurement deviations for different heights of the TX and the RX stay within the measurement accuracy of 3 dB for the amplitude and 0.5 ns for the delay that is estimated from observation. Thus, the height does not produce any noticeable effect on the path loss, even for the case where both TX and RX antennas are located at the bumper level ($h = 0.4$ m). As there is no significant difference between the considered heights, we present the curve averaging the measured values for the same distances, thus reducing the effect of the measurement error before we proceed with the path loss modeling.

Proceeding with the path loss modeling, we note that the observed behavior advocates the use of conventional Friis free space path loss (FSPL) that depends on the propagation distance and carrier frequency. To this aim, Fig. 5 illustrates the FSPL approximation that accounts for the TX and the RX antenna gains. As one may observe, the averaged measurement data underestimate the theoretical results of the FSPL across all the considered values of d by, on average, 1.04 dB. These additional losses can be attributed to the imperfectness of measurement conditions and beam alignment between the TX and the RX. Introducing the correcting factor, $C_{\text{corr}} = 1.04\,\text{dB} \approx 1\,\text{dB}$, our measurement study reveals that the path loss over a LoS link between the TX and the RX, $L_{\text{dB}}(d)$, can be approximated by a FSPL equation in the following form

$$L_{\text{dB}}(d) = 20\log_{10}(d) + 20\log_{10}(f) - 147.55 + C_{\text{corr}}\,, \quad (6)$$

where f stands for the frequency of 304.2 GHz and C_{corr} accounts for the extra attenuation caused by the imperfect alignment of the TX and the RX antennas. We also note that almost all the measurement data lie in between the results predicted by FSPL model and FSPL model plus 3 dB, thus ensuring the confidence in the accuracy of the measured data.

Here, we recall that many of the corresponding studies for mmWave systems report the path loss exponent other than two (typically, in the range of 1.7–2.7) [29]–[32]. However, these models are built for much longer distances and also subject to the effects caused by the signal reflection from multiple sources (i.e., buildings), as well as possible signal blockage by vehicle bodies and other obstacles. Hence, these mmWave-specific models cannot be used as LoS reference data for our further measurement results.

Following a close match between our measured values and their analytical approximation presented in (6), we apply the results from (6) further in our analysis as the reference data.

B. Vehicle-Body Blockage

In this subsection, we proceed by exploring the impact of vehicle-body blockage on the low THz channel. We particularly investigate a setup, where the LoS between the two communicating cars is occluded by a vehicle that does not participate in the ongoing communication, as illustrated in Fig. 6. Here, the IRs are recorded for a height of the TX and the RX antennas $h > 0.9$ m and different separation distances between TX and RX, d, from 6 m to 12 m.

Fig. 7 illustrates the measurement results for this setup. The figure presents the additional losses introduced by the vehicle-body blockage – on top of the LoS propagation loss estimated with (6).[1] A particular emphasis is on exploring

[1]An alternative approach here may be to move the vehicle after each of the measurements so that the blockage data can be directly compared to the reference measurement data for the same distance. However, this approach is more challenging, as it requires moving the heavy SUV in and out multiple times. It also demands the vehicle to be returned to the same location with the cm-scale precision, as the curvature of the car body starts having an impact.

the losses when propagating through the vehicle at the window level with $h \in [1.25\text{ m}; 1.55\text{ m}]$. We also report the losses of propagating through side windows of the VUT for both front side windows and rear side windows with $h \in [1.25\text{ m}; 1.75\text{ m}]$.

Analyzing Fig. 7, one first observes that the losses caused by the vehicle-body blockage highly depend on h. In addition, the dependency is strongly non-monotonic featured by high losses at the engine level: around 40 dB for $h \approx 1$ m and 50 dB for $h \approx 1.2$ m. At the windshield level ($h \approx 1.25$ m) the losses drop by almost 20 dB and then grow again to approximately 45 dB for $h \approx 1.4$ m. We also observe that the additional path loss for $h > 1.65$ m is slightly negative, primarily due to the reflection from the rooftop arriving at the same delay bin. Here, the flat metallic roof of the vehicle serves as a good reflector, concentrating the THz waves towards the receiver. Such a non-monotonic behavior can be explained by the heterogeneity of the materials and geometrical configurations that the low THz signal has to propagate through at different heights. The observed effect challenges the accurate modeling of the vehicle-body blockage effect, as the blockage model becomes considerably more difficult than the corresponding models utilized, e.g., for the human-body blockage, where the entire human body is typically approximated with a cylinder featured by homogeneous losses [33].

It is also important to note that the propagation loss through a pair of windows of ≥ 30 dB is significantly larger than the loss of 3 dB caused by the propagation through a single glass window [34]. This effect is explained by the curved shape of the vehicular windows and, primarily, by the multipath propagation inside the cabin with multiple reflection and penetration losses from the seats, head restraints, and other interior objects present.

Note that the observed losses of up to 50 dB are considerably higher than the values reported earlier for lower frequencies, implying that no effective communications in the low THz band are possible through the vehicle body at the engine level. In contrast, only 5 dB to 30 dB excess blockage loss has been observed for 60 GHz, depending on the blocker size and the number of intermediate vehicles [29]. The corresponding height-dependent losses for 28 GHz are: 30 dB to 40 dB for 0.6 m, 13.3 dB for 1.5 m, and 11 dB to 12.2 dB for 1.7 m that qualitatively agree with our data [35]–[37].

Summarizing the findings of this section, the vehicle-body blockage is observed to be a major factor that must be accounted for in the design and evaluation of the prospective vehicular communication systems in the low THz band.

C. Under-Vehicle Propagation

We continue our study on the vehicle-body blockage by exploring a specific setup, where the low THz signal propagates not through but rather under the vehicle body. This communications scenario is of particular interest when the path between TX and intended RX is blocked by another vehicle that does not allow for relaying. As briefly discussed at the end of Subsection II-A, this component simultaneously characterizes the interference induced by a TX–VUT link to a link between the VUT and the RX.

(a) Measurement Setup

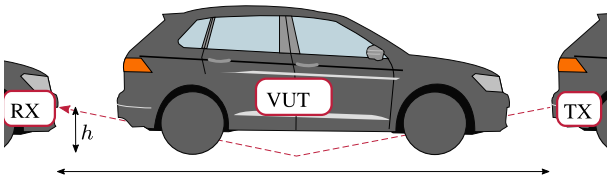

(b) Schematic view

Fig. 8. Setup for the under-vehicle propagation.

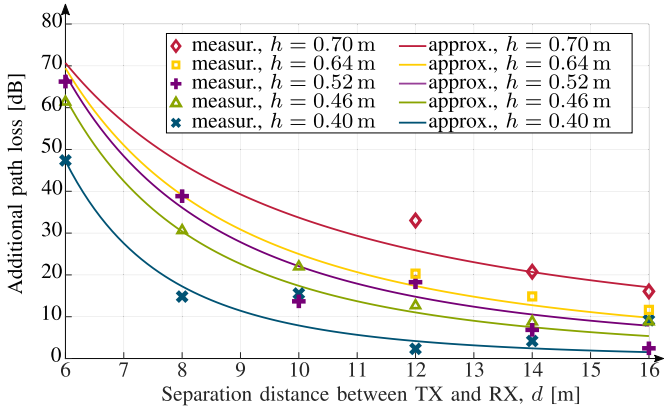

Fig. 9. Measured and modeled loss for under-vehicle propagation.

The measurement setup for under-vehicle propagation is illustrated in Fig. 8. The main parameter of interest here is the separation distance between the TX and the RX, d. Note that in real conditions, the minimum value of d is limited to the length of the VUT plus the safety distance to the preceding and the following vehicles. Thus, we start our measurements at 6 m that roughly corresponds to the traffic jam conditions in an urban scenario. The maximum separation distance is set to 16 m representing normal street traffic conditions or a packed highway scenario. The blocking VUT is always positioned halfway between TX and RX. In this setup, contrarily to the unobstructed LoS conditions, one may expect that the height of the TX and RX may also notably affect the path loss. For this reason, in addition to the distance-related parameters explained above, we measured the under-vehicle propagation at multiple different heights $h < 0.9$ m.

The obtained results are illustrated in Fig. 9, presenting the additional path loss on top of the FSPL model from Subsection III-A as a function of the distance between TX and RX. We specifically note that due to the geometry of the under-vehicle propagation only data points for distances

TABLE I

COEFFICIENTS α AND β USED TO APPROXIMATE THE UNDER-VEHICLE PROPAGATION LOSSES IN (7)

h [m]	α	β	h [m]	α	β
0.4	23000	3.4	0.7	820	1.35
0.46	4800	2.4	0.76	580	1.15
0.52	3000	2.1	0.82	450	1.0
0.64	1800	1.8	0.88	350	0.85

greater than 10 m are available when TX and RX heights are higher than 0.64 m. Analyzing the presented data, one may observe that the range of absolute values of additional losses is extremely large, varying from as low as 0.5 dB to as high as 64 dB and tending to match the results for the vehicle-body blockage for shorter distances. The additional path loss also decreases with d for all considered TX and RX heights. The reason is that even in spite of very small utilized HPBW, a part of the low THz signal still propagates under the VUT, and this portion increases with the distance. The decay highly depends on the heights of TX and RX and is non-linear (even in decibel scale) that has to be accounted for when developing the corresponding propagation and interference models.

The reported results advocate for the following structure of the path loss model in vehicle blockage conditions. First, the power-law function needs to be utilized to capture the dependency between the additional path loss and the separation distance d. Furthermore, depending on the RX and TX heights, additional parameters need to be introduced, specifying the height and the shape of the path loss curve. Uniting this model with the LoS propagation loss formula, the model expressing the total path loss can be approximated as

$$L_{\text{dB}}(d,h) = 20\log_{10}(d) + 20\log_{10}(f) - 147.55 + C_{\text{corr}} + \mathbb{1}\left(\alpha d^{-\beta}\right), \quad (7)$$

where $\mathbb{1}(\cdot)$ is the indicator function that takes on 1 in case of the vehicle-body blockage and 0 otherwise, while α and β are the coefficients accounting for the TX and the RX heights. Here, the mean squared error is particularly applied as a criteria to determine these coefficients. The calculated values of α and β are presented in Table I.

The results produced with (7) are also illustrated in Fig. 9 demonstrating a tolerable match between the measurement data and the proposed approximation. Hence, for typical heights of the TX and RX antennas, the complex effect of under-vehicle propagation losses can be well approximated with an analytical expression. These results can be further refined in follow-up in-depth studies exploring the impact of different road surfaces on THz band vehicular communications, i.e., by extending the methodology developed for mmWave vehicular systems in [22].

D. Single-Lane Front and Rear Reflection

The last investigated setup in this section refers to a standard communication scenario where two cars drive one after another. Since a major part of vehicles is made out of metals,

(a) Measurement setup

(b) Schematic of rear reflection (c) Schematic of front reflection

Fig. 10. Setup for the single-lane front and rear reflection.

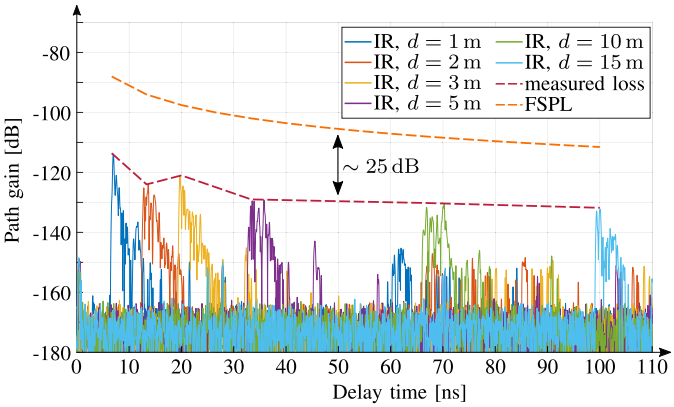

Fig. 11. Reflection from the front of the VUT.

a significant reflection from the VUT can be expected that might cause self-interference at the RX. Fig. 10 shows the setup of the radar-like measurements, aiming to explore the levels of self-interference in different configurations. Here, TX and RX are both set to a height of 58 cm and the IR is captured for the distances $d = \{1, 2, 3, 5, 10, 15\}$ m between TX and the VUT. The measurements are performed for both rear and front sides of the VUT, as illustrated in Fig. 10b and Fig. 10c.

We start to characterize this scenario with Fig. 11 that shows the IRs of the propagation channel reflecting from the front part of the vehicle. For the considered setup, we are also interested in delay-dependent characteristics. Thus, we analyze the IR before proceeding to the path loss study. As one may observe from Fig. 11, for each distance the IR shows one major component that can be characterized by a striking peak followed by a decrease within 10 ns. Although the structure of the pulse is not identical for the different distances, the envelope of the pulse shape shows a similar form. The enlargement of the pulse equals to a geometric dimension of 3 m that is in the order of magnitude of the length of the VUT. Thus, the whole vehicle body contributes to the reflection. In addition, Fig. 11 shows the contribution of the FSPL to the overall path loss as a function of the distance that is translated to a delay by the speed of light. The path loss of the main peak varies between -113 dB and -130 dB and shows a decreasing trend with distance. It is notable that

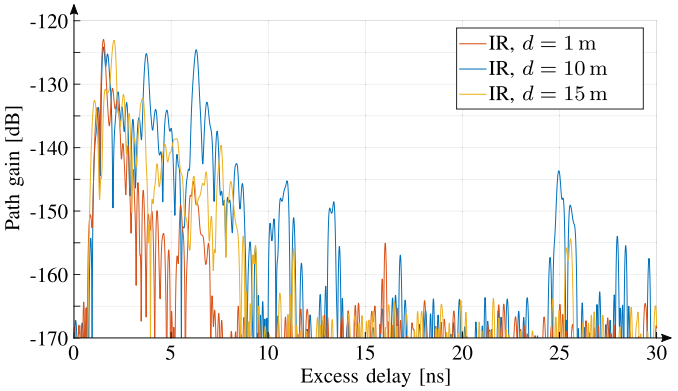

Fig. 12. IRs for the reflection from the rear side.

(a) Measurement setup

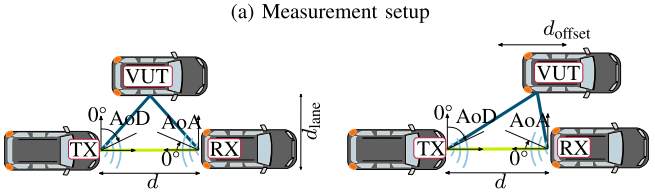

(b) Schematic of symmetric side reflection setup

(c) Schematic of asymmetric side reflection setup

Fig. 13. Setup for the side reflection. LoS path is green, while the side reflection path is blue.

the difference between the path loss and the contribution of the FSPL stays constant and thus leads to a constant reflection loss at the vehicle of ∼25 dB.

To characterize rear reflection, Fig. 12 visualizes the IRs of the reflection at the rear side of the VUT for different distances as a function of the excess delay. As one may observe comparing the IRs from Fig. 11 and Fig. 12, no major difference is visible and the characteristics for the reflection from the front also hold for the rear side of the vehicle. The measurements show the lowest RMSDS of 0.73 ns and the highest RMSDS of 2.44 ns with an average RMSDS of 1.22 ns. For the RMSDS calculation the direct leakage at 0 ns between TX and RX is canceled out and the IRs are cut off at 25 ns to reduce the influence of the noise. Comparing the impact of the potential interference channel to the FSPL of the corresponding communication link with distance d, a signal-to-interference ratio (SIR) of 17 dB to 25 dB is obtained for a distance d greater than 3 m. Therefore, in certain configurations this component may limit the capacity of the communication link and should be considered in future system design.

IV. Multi-Lane Analysis and Modeling

Having characterized the path loss models for a single-lane environment we now proceed with describing more sophisticated propagation components for multi-lane scenarios. Particularly, we concentrate on side-reflection and multi-lane front and rear reflection setups.

A. Symmetric Side Reflection

Depending on the considered communications scenario, side reflection may be considered as unwanted interference component or as a useful propagation path. As an interference path, the side reflection component can occur on almost all streets, multi-lane as well as bi-directional traffic scenarios. Given an active link between two vehicles driving one after another, a vehicle on the adjacent lane that is represented by the VUT, affects the propagation channel. The side reflection setup investigates this inevitable reflection from the vehicle at the neighboring lane that might lead to intersymbol interference (ISI). Alternatively, one may utilize side reflection as an additional useful propagation path bypassing the vehicle up front when the under-vehicle propagation path is insufficient for reliable communications.

TABLE II
Multipath Characteristics for Side Reflection

direct path		reflected path			
d [m]	delay [ns]	rel PL [dB]	delay [ns]	AoD [°]	AoA [°]
2	6.43	12.5	19.04	24	72
4	13.27	13.3	22.38	40	56
6	19.93	4.9	26.96	48	40
8	26.40	5.0	31.98	56	32
10	33.12	6.4	37.86	56	32
12	39.66	3.4	43.63	64	24

1) Setup and Observations: The considered measurement setup for this scenario is illustrated in Fig. 13. Here, we are interested in the characteristics of the propagation path reflected at the side of a vehicle located in the neighboring lane. To this aim, we first vary the separation distances d between TX and RX from 2 m to 12 m, where the VUT stays at a centered position resulting in a symmetric setup (see Fig. 13b). TX and RX are installed on rotational units to scan the angle from 0° to 88° allowing us to obtain the PAP. As the HPBW of the used antennas is 8.5°, a rotation step of 8° was selected, so that all notable MPCs may be captured with an error of less than 3 dB [38]. The IR is cut at 50 ns that equals a path length of 15 m to eliminate the hall influence.

In all the considered setups two MPCs can be observed: (i) the direct path between TX and RX plus (ii) a significant first order reflection from the VUT. Table II summarizes the measured delay of the two MPCs, the relative path loss of the reflected path normalized to the path loss of the direct path, as well as its AoD and AoA.

We start to investigate the considered scenario by visualizing the measurements with the help of the PAP and the ODIR introduced in Section II. To this aim, Fig. 14 illustrates the PAPs for $d = \{2, 6, 12\}$ m and Fig. 15 the corresponding ODIRs. The direct path stays constant at an $(\varphi_{\text{AoD}}|\varphi_{\text{AoA}}) = (88°|0°)$. The ODIRs show that the delay of the direct path increases as expected corresponding to the increase of distance. It is also notable, that the first order reflection at the

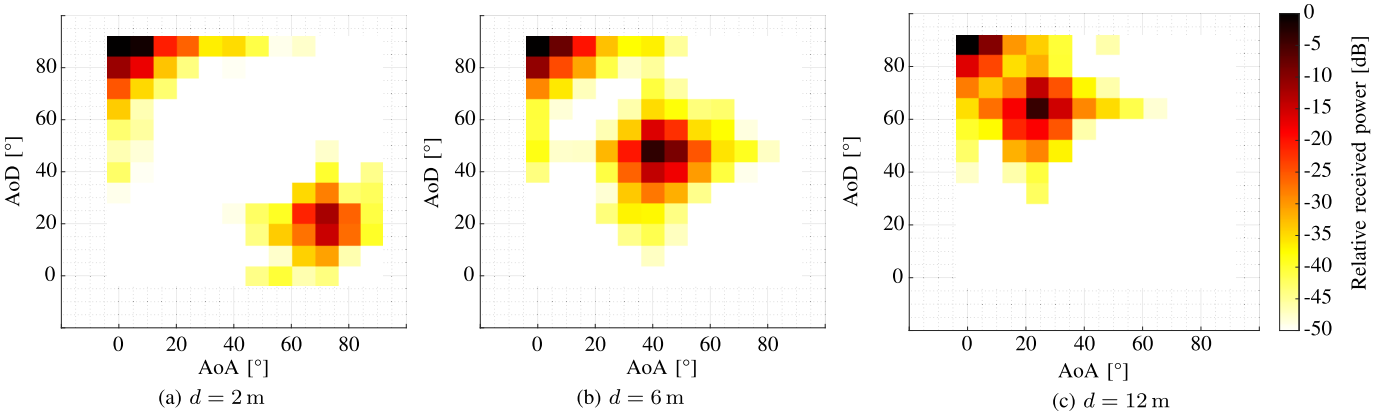

Fig. 14. PAP of the symmetric side reflection for different distances between TX and RX.

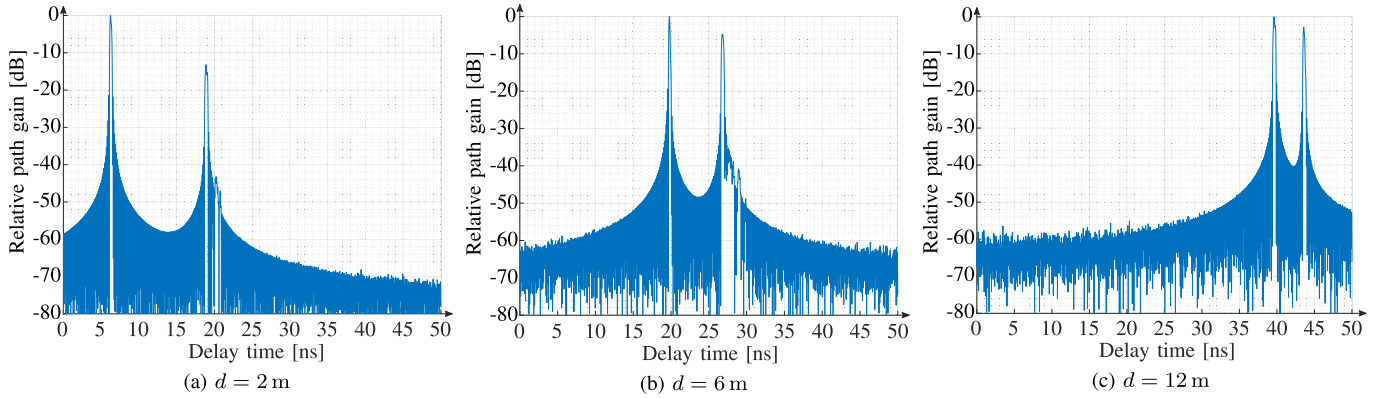

Fig. 15. ODIR of the symmetric side reflection for different distances between TX and RX.

VUT is clearly visible as a sharp specular reflection point. With the increased distance the reflection moves closer to the direct path in the spatial domain. The difference in delay and the relative path loss decrease with the increased distance augmenting the influence of the MPC for greater distances.

2) Two-Ray Model Approximation: All three abovementioned trends are in line with the geometrical changes in the setup. To further investigate and explain the dependencies and impacts, we model MPCs utilizing a ray-based approach. From the PAP and the ODIR two MPCs were clearly identified. The direct path is attributed to the direct link between TX and RX while the reflected path is associated with the path from TX to the center of the side of the VUT ending at the RX. Both paths are schematically visualized in Fig. 13b, where the direct path is drawn in light green and the reflected path is blue. The two paths are combined in the IR as follows

$$h(t,\tau) = \frac{1}{c_{\mathrm{LoS}}(t)}\delta[\tau - \tau_{\mathrm{LoS}}(t)] + \frac{1}{c_{\mathrm{refl}}(t)}\delta[\tau - \tau_{\mathrm{refl}}(t)]\,, \quad (8)$$

where $\tau_{\mathrm{LoS}}(t)$ and $\tau_{\mathrm{refl}}(t)$ denote the delay of the respective path and are provided by

$$\tau_{\mathrm{LoS}}(t) = \frac{d_{\mathrm{LoS}}}{c}\,, \quad \tau_{\mathrm{refl}}(t) = \frac{d_{\mathrm{refl}}}{c}\,, \quad (9)$$

and c_{LoS} and c_{refl} denote the linear path loss of the direct path and the reflected path, respectively, as illustrated in Fig. 13b. Hence, the distances d_{LoS} and d_{refl}, where

$$\begin{aligned} d_{\mathrm{LoS}} &= |\mathbf{r}_{\mathrm{RX}}(t) - \mathbf{r}_{\mathrm{TX}}(t)|\,, \\ d_{\mathrm{refl}} &= |\mathbf{r}_{\mathrm{VUT}}(t) - \mathbf{r}_{\mathrm{TX}}(t)| + |\mathbf{r}_{\mathrm{RX}}(t) - \mathbf{r}_{\mathrm{VUT}}(t)|\,, \end{aligned} \quad (10)$$

the AoD and the AoA are determined based on the TX position $\mathbf{r}_{\mathrm{TX}}(t)$, the RX position $\mathbf{r}_{\mathrm{RX}}(t)$, and the point of reflection of the VUT $\mathbf{r}_{\mathrm{VUT}}(t)$.

Utilizing the results of Section III, the loss of the direct path is modeled with FSPL as follows

$$c_{\mathrm{LoS,dB}} = 20\log_{10}(d_{\mathrm{LoS}}) + 20\log_{10}(f) - 147.55 + C_{\mathrm{corr}}\,. \quad (11)$$

Moreover, due to the reflection at the VUT, an additional reflection loss C_{RL} is added to the path loss of the reflected path as provided below resulting in

$$\begin{aligned} c_{\mathrm{refl,dB}} = {} & 20\log_{10}(d_{\mathrm{refl}}) + 20\log_{10}(f) \\ & - 147.55 + C_{\mathrm{corr}} + C_{\mathrm{RL}}\,. \end{aligned} \quad (12)$$

The reflection loss C_{RL} on the side of the vehicle is further extracted from the side reflection measurements by subtracting the difference of the FSPL of the direct path and the reflected path from the relative path loss of the reflected path. The reflection loss appears to be constant with an average reflection loss of 5.0 dB and a minimum reflection loss of 2.4 dB. Since the measured path loss can be higher than the actual

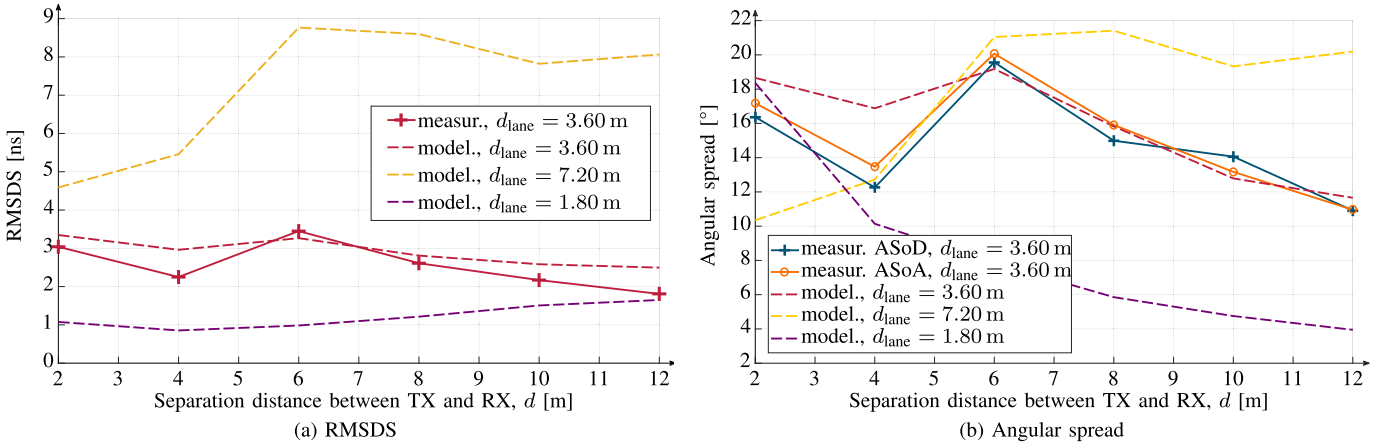

(a) RMSDS (b) Angular spread

Fig. 16. RMSDS, ASoD, and ASoA for the side reflection.

path loss because of alignment and positioning inaccuracies, the minimum reflection loss should be considered in link- and system-level simulations.

3) Evaluation of Spreads and Coherence Bandwidth: To evaluate the validity of the model the RMSDS, the ASoD and the ASoA are calculated as a figure of merit based on the measurements and the model. For this purpose a synthetic discrete IR with the same sampling interval and noise characteristics as the measurement data was created. Furthermore, the side distance d_{lane} (the distance between the vehicles in the neighboring lanes as illustrated in Fig. 13b) is varied from half of the standard lane width in traffic jam situations to twice of the standard lane width when a vehicle doubles at the next-to-adjacent lane in order to assess the value range of the simulated data.

The results are presented in Fig. 16, where the RMSDS in Fig. 16a starts at 3.04 ns showing a decreasing trend. The modeled data start at 3.35 ns and also shows the decreasing trend but with lower variations. The variations of the measured RMSDS (i.e., at $d = 4$ m), which are linked to the reflection loss, may originate from an angular dependent reflection coefficient or positioning and alignment inaccuracies, as explained above. To better understand the trend of the spreads we have to take a closer look. The RMSDS and the angular spread are affected by two competing mechanisms. On one hand, the decreasing angular difference in Fig. 14 and the difference in delay in Fig. 15 lead to a smaller spread. At the same time, the decreasing power difference of the two MPCs increases the spread. Here, the proposed model can provide a quantification and help to determine the dominating effect and the trend in the respective setup.

Another figure of merit is the coherence bandwidth B_{coh} that represents the bandwidth for which the spaced-time spaced-frequency correlation function reaches half of its maximum and can be approximated by [39]

$$B_{\text{coh}} \approx \frac{1}{5\tau_{\text{DS}}} . \tag{13}$$

For the reported measurements, the coherence bandwidth of the considered low THz link varies from 66 MHz to 110 MHz. Therefore, in the context of low THz communications, where a bandwidth of tens of GHz will be utilized, the propagation channel cannot be assumed to be flat. So even if the RMSDS decreases with distance, the MPCs tend to get closer in power (difference of only 3.4 dB), in delay (4.0 ns) and in the angular domain (24°). Ultimately, the impact of this effect heavily depends on the employed antenna with its individual side lobes and features, especially, for beam steerable antennas.

Proceeding with the investigation of the influence of the side distance, the model shows a higher RMSDS for twice the standard lane width $d_{\text{lane}} = 7.20$ m with a decreasing trend for greater separation distances d. In contrast, the smaller side distance $d_{\text{lane}} = 1.80$ m shows an increasing trend. So, in comparison to the results for other side distances the model and the measurement data match well for $d_{\text{lane}} = 3.60$ m.

The same observations is made for the angular spread in Fig. 16b. Here, the model and the measured data have a good agreement especially for distances higher than 4 m. The higher deviation at $d = 4$ m can be explained by the relatively high path loss measured at this distance. This inaccuracy may also be linked to the imperfections of the positioning and the limited angular resolution. Our measurements demonstrate RMSDS of 2 ns to 3 ns, which is in the same order of magnitude with RMSDS of 3.35 ns reported earlier for 60 GHz in [40]. Note that our setup and the setup in [40] are comparable only in a broad sense, therefore, a perfect match is not anticipated. Regarding the observed influence of the lane width, the angular spread also increases with the lane width as does the RMSDS.

B. Asymmetric Side Reflection

The asymmetric reflection measurements aim at investigating the influence of the side reflection through scattering when no specular reflection is available. It also mirrors the effects during an overtaking procedure. For this reason, TX and RX remains at a distance $d = 12$ m and the VUT is moved by an offset distance d_{offset} from 0 m to 6 m in steps of 2 m in the direction of travel, see Fig. 13c. The measured data are summarized in Table III. Analyzing these data, one may observe that the path loss drops significantly by 7 dB when the VUT is moved by just 2 m. Recalling that the length of the VUT of 4489 mm, we note that a specular reflection is still possible in these conditions and the reflection point stays

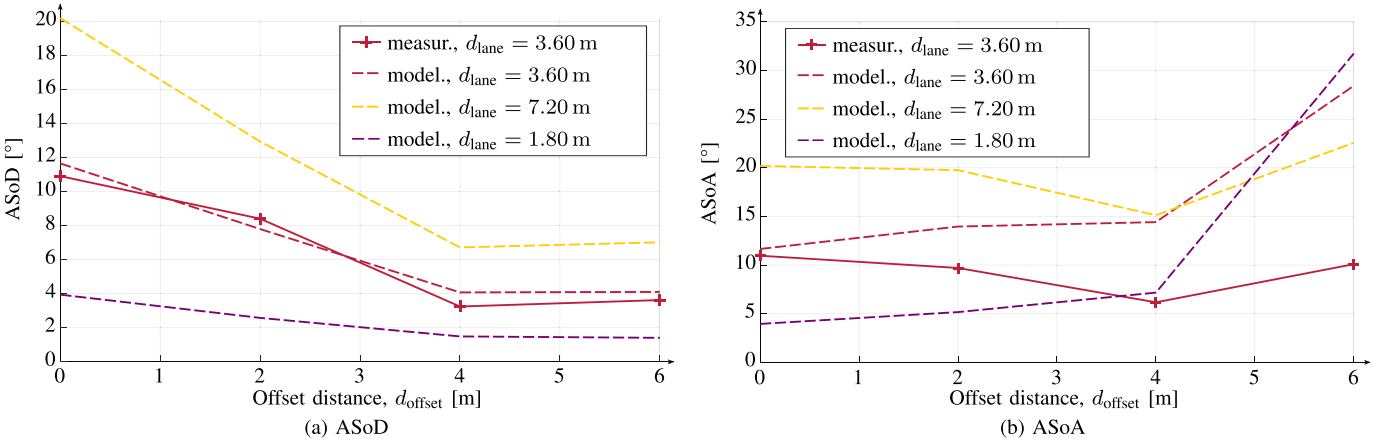

(a) ASoD (b) ASoA

Fig. 17. ASoD and ASoA for asymmetric side reflection.

TABLE III
MULTIPATH CHARACTERISTICS FOR ASYMMETRIC SIDE REFLECTION MEASUREMENTS, $d = 12$ m

direct path		reflected path			
d_{offset} [m]	delay [ns]	rel PL [dB]	delay [ns]	AoD [°]	AoA [°]
0	39.66	3.4	43.63	64	24
2	39.66	10.4	43.79	64	24
4	39.66	20	44.29	72	40
6	39.66	16.0	46.36	72	56

approximately at the same absolute position which is also supported by the similar delay, AoD and AoA. Augmenting the offset distance even further leads to another significant drop of 6 dB to 10 dB, when no specular reflection is possible anymore. Thus, the scattered components are estimated to be 16 dB to 20 dB below the specular component.

In the asymmetric side reflection scenario, the behavior of the angular spread requires careful investigation. To this aim, the ASoD and ASoA are plotted in Fig. 17. As one may observe, the proposed two-ray model catches the decreasing trend of the ASoD well and agrees with the measurements, whereas the ASoA is slightly overestimated for greater offset distances. From the measured AoD and AoA provided in Table III we observe that the point of reflection shifts to the rear part of the VUT whereas the model always uses the center of the vehicle as the point of reflection. The modeled MPC is therefore characterized by a greater AoA than the real component leading to larger values of ASoA. The RMSDS shows a decreasing trend from 1.8 ns to 1.4 ns for an offset distance of 2 m and 6 m, respectively. Thus, we conclude that the two-ray model also slightly overestimates the RMSDS based on the measured data by up to 2 ns because of the same effect: the modeled path length and the associated delay are both longer than those of the actual path. In spite of these imperfections, the utilized two-ray model still captures the major effects in the considered propagation environment.

C. Multi-Lane Front and Rear Reflection

The last considered setup of the measurement campaign is the multi-lane front and rear reflection. In this scenario, TX and the VUT are assumed to drive one after another on the same lane having an active communication link. We are interested in the channel that RX sees when driving on the neighboring lane. This can be of interest when estimating the lane-to-lane interference or the interference in case of a side lane link when RX wants to establish a communication link with the VUT.

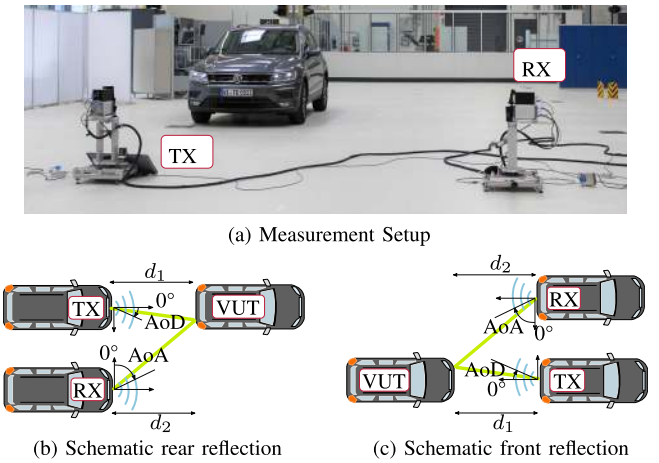

(a) Measurement Setup

(b) Schematic rear reflection (c) Schematic front reflection

Fig. 18. Setup for multi-lane front and rear reflection.

The considered setup is visualized in Fig. 18, where d_1 denotes the distance between TX and the VUT. On its turn, d_2 defines the distance between the VUT and RX. For $d_1 = 1$ m, $d_1 = 5$ m, and $d_1 = 10$ m the configurations $d_2 = \{1, 2, 3, 4\}$ m, $d_2 = \{1, 3, 5, 10\}$ m, and $d_2 = \{1, 5, 10, 15\}$ m are measured, respectively. This is done for TX and RX looking both towards the front side of the VUT (see Fig. 18b) and towards the rear side of the VUT (see Fig. 18c), respectively. In both cases, TX is rotated in the range of $\varphi_{\text{AoD}} = [0, 16]°$ and RX is rotated in the range of $\varphi_{\text{AoA}} = [0, 88]°$ both again with a step size of 8° corresponding to the HPBW of the utilized horn antenna. Here, to cancel out the effects originating from the environment, the IR is cut off at 90 ns. This corresponds to 27 m accounting for the longest possible path in the investigated scenario.

Observing the PAP illustrated in Fig. 19 it is notable that the beam of the scattered components is more enlarged compared to the specular reflection from the previous side reflection

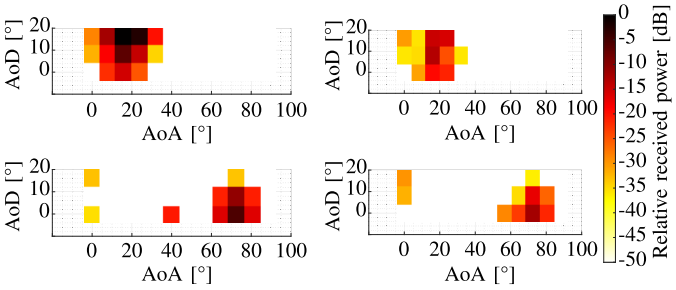

(a) Reflections from the rear (b) Reflections from the front

Fig. 19. Selected PAPs for multi-lane front/rear reflection: $d_1 = 1\,\text{m}$; $d_2 = 1\,\text{m}$ (top); $d_1 = 10\,\text{m}$; $d_2 = 10\,\text{m}$ (bottom).

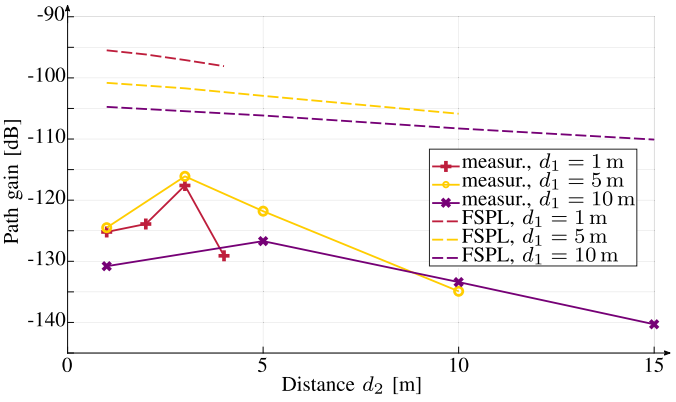

(a) Reflection from the rear side

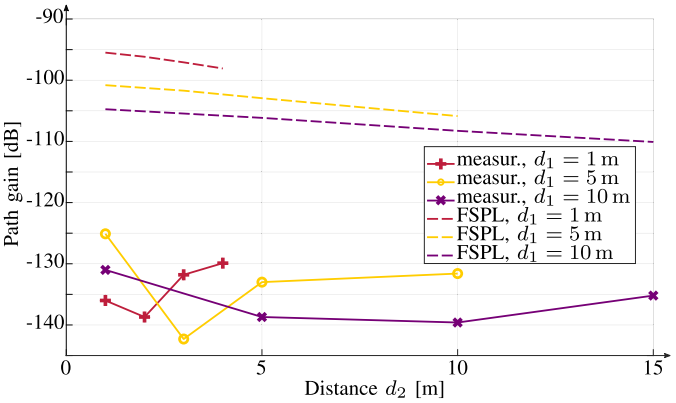

(b) Reflection from the front side

Fig. 20. Path loss for multi-lane front and rear reflection.

setup. In five cases two neighbor measurement points in the PAP vary less than by 1 dB that leads to the conclusion that the reflection coefficient is constant over the width of the VUT. The AoD and AoA of the scattered path behave as expected from the geometry of the setup. Particularly, increasing d_1 from 1 m to 5 m and later to 10 m decreases the AoD from 16° to 8° and later to 0°, respectively. Correspondingly, the AoA increases up to 80° for d_2 equal to 15 m. Another noteworthy fact is that the combinations of AoD and AoA are equal for the front and the rear setup.

The absolute path loss lies between -116 dB and -142 dB and is visualized in Fig. 20. For comparison purposes also the path loss originating from the FSPL is added to the illustration. One may observe that the reflection from the rear side of the VUT is more powerful than the reflection from the front. Also, the front and the rear side are characterized by different trends. While the reflection from the front shows a convex curve, the reflection from the rear has a concave appearance. Subtracting the FSPL part from the path loss, a reflection loss of 15 dB to 30 dB is obtained for the reflection from the rear side of the VUT. Similarly, the reflection from the front side results in a higher loss from 24 dB to 42 dB. We note that directive antennas can reduce the influence of the multi-lane front and rear reflections. However, in the case of beam steerable antennas the impact of high side lobes still have to be considered.

Note that the reflection loss of the front and rear reflection in the multi-lane scenario is much higher compared to the reflection loss of the side reflection (2.4 dB) reported above. The origin for this effect is related to the irregular shape of the front and rear side of the VUT and the specific materials utilized for these parts of the vehicle. Particularly, the side doors of the VUT are made of steel and the front and rear side is dominated by the plastic bumper and the radiator grill.

V. Conclusion

High-rate vehicular networking is one of the promising usage scenarios for prospective beyond 5G communication systems in the low THz band. In this article, we report a comprehensive measurement study of low THz signal propagation at 300 GHz in both single-lane and multi-lane vehicular environments. Our study reveals that vehicular communications over these frequencies are characterized by complex multi-path propagation with several components having different importance for prospective communications.

We particularly observe that the vehicle body is a strong blocker of low THz radiation resulting in 30 dB to 50 dB additional loss on top of the line-of-sight propagation. The penetration loss notably depends on the height of the incident signal when propagating through the vehicle. We also reveal that the characteristics of the low THz signal propagation under the vehicle body heavily depend on the distance between the transmitting and the receiving vehicles, as well as the heights of the TX and RX antennas. Particularly, the under-vehicle propagation can be ignored for a hood-level location of the antennas and shorter TX-RX distances, while it must be accounted when the antennas are located at a bumper level, and the distance between the communicating vehicles is larger than 8 m. Finally, we note the non-negligible impact of the signal reflections from the sides of the vehicle with a loss of around 3 dB, while the impact of signal reflection from the front and the rear of the vehicle is of secondary importance featured by approximately 25 dB extra attenuation. Based on the temporal and spatial analysis, a two-ray model presents a good approximation for the delay spread and angular spread. Whenever applicable, the delivered results are compared to the findings on mmWave vehicular communications showing similarity in some metrics (i.e., RMSDS) and non-negligible differences in others (i.e., losses due to vehicle-body blockage).

TABLE IV

REVEALED APPROXIMATIONS FOR DIFFERENT EFFECTS IN LOW THZ BAND VEHICULAR COMMUNICATIONS AT 300 GHZ

Setup	Model
	Single-lane scenarios
LoS propagation	FSPL
Vehicle-body block.	FSPL + height-dependent penetration loss of 30 dB to 50 dB. *Important to account for in the analysis.*
Under-vehicle prop.	FSPL + $\alpha d^{-\beta}$, where α and β are as in Table I. *Important to account for in the analysis.*
Front/rear reflection	FSPL + reflection loss of $\sim$25 dB. *May be neglected in first-order studies.*
	Multi-lane scenarios
Sym. side reflection	Two-ray model approximation: FSPL + reflection loss of $\sim$3 dB. *Important to account for in the analysis.*
Assym. side reflection	Two-ray model approximation: FSPL + angle-dependent loss of 16 dB to 20 dB. *May be neglected in first-order studies.*
Front reflection	Two-ray model approximation: FSPL + angle-dependent loss of 24 dB to 42 dB. *May be neglected in first-order studies.*
Rear reflection	Two-ray model approximation: FSPL + angle-dependent loss of 15 dB to 30 dB. *May be neglected in first-order studies.*

Further observations for link-level and system-level modeling of low THz vehicular communications are summarized in Table IV. The contributed results present a baseline for further in-depth measurement studies on THz vehicular networks in more complex environments, i.e., heterogeneous road surfaces, urban streets and foliage, multiple different and mobile vehicles. The obtained measurement results and their analysis, together with the contributed approximations, may also serve as building blocks when developing scenario-specific link- and system-level simulations for prospective vehicular communication systems in the low THz band.

REFERENCES

[1] T. S. Rappaport *et al.*, "Wireless communications and applications above 100 GHz: Opportunities and challenges for 6G and beyond," *IEEE Access*, vol. 7, pp. 78729–78757, Jun. 2019.

[2] *World Radiocommunication Conference 2019 (WRC)—Provisional Final Acts*, ITU Publications, Int. Telecommun. Union Radiocommun. Sector, Geneva, Switzerland, Mar. 2020.

[3] Q. Bi, "Ten trends in the cellular industry and an outlook on 6G," *IEEE Commun. Mag.*, vol. 57, no. 12, pp. 31–36, Dec. 2019.

[4] I. F. Akyildiz, J. M. Jornet, and C. Han, "Terahertz band: Next frontier for wireless communications," *Phys. Commun.*, vol. 12, pp. 16–32, Sep. 2014.

[5] I. F. Akyildiz, C. Han, and S. Nie, "Combating the distance problem in the millimeter wave and terahertz frequency bands," *IEEE Commun. Mag.*, vol. 56, no. 6, pp. 102–108, Jun. 2018.

[6] V. Petrov, M. Komarov, D. Moltchanov, J. M. Jornet, and Y. Koucheryavy, "Interference and SINR in millimeter wave and terahertz communication systems with blocking and directional antennas," *IEEE Trans. Wireless Commun.*, vol. 16, no. 3, pp. 1791–1808, Mar. 2017.

[7] J. Edstam, J. Hansryd, S. Carpenter, T. Emanuelsson, Y. Li, and H. Zirath, "Microwave backhaul evolution—Reaching beyond 100 GHz," *Ericsson Technol. Rev.*, no. 2, Oct. 2017. [Online]. Available: https://www.ericsson.com/en/reports-and-papers/ericsson-technology-review/articles/microwave-backhaul-evolution-reaching-beyond-100ghz

[8] *IEEE Standard for High Data Rate Wireless Multimedia Networks Amendment 2: 100 Gb/s Wireless Switched Point-Topoint Physical Layer*, Standard 802.15.3d–2017, IEEE, Institute of Electrical and Electronics Engineers, 2017.

[9] M. Giordani, M. Polese, M. Mezzavilla, S. Rangan, and M. Zorzi, "Toward 6G networks: Use cases and technologies," *IEEE Commun. Mag.*, vol. 58, no. 3, pp. 55–61, Mar. 2020.

[10] S. Mumtaz, J. M. Jornet, J. Aulin, W. H. Gerstacker, X. Dong, and B. Ai, "Terahertz communication for vehicular networks," *IEEE Trans. Veh. Technol.*, vol. 66, no. 7, pp. 5617–5625, Jul. 2017.

[11] J. Choi, V. Va, N. Gonzalez-Prelcic, R. Daniels, C. R. Bhat, and R. W. Heath, Jr., "Millimeter-wave vehicular communication to support massive automotive sensing," *IEEE Commun. Mag.*, vol. 54, no. 12, pp. 160–167, Dec. 2016.

[12] V. Petrov, D. Moltchanov, S. Andreev, and R. W. Heath, Jr., "Analysis of intelligent vehicular relaying in urban 5G+ millimeter-wave cellular deployments," in *Proc. IEEE Global Commun. Conf. (GLOBECOM)*, Dec. 2019, pp. 1–6.

[13] V. Petrov, T. Kurner, and I. Hosako, "IEEE 802.15.3d: First standardization efforts for sub-terahertz band communications toward 6G," *IEEE Commun. Mag.*, vol. 58, no. 11, pp. 28–33, Nov. 2020.

[14] T. Kürner, A. Fricke, S. Rey, P. L. Bars, A. Mounir, and T. Kleine-Ostmann, "Measurements and modeling of basic propagation characteristics for intra-device communications at 60 GHz and 300 GHz," *J. Infr., Millim., THz Waves*, vol. 36, no. 2, pp. 144–158, Feb. 2015.

[15] N. Khalid and O. B. Akan, "Wideband THz communication channel measurements for 5G indoor wireless networks," in *Proc. IEEE Int. Conf. Commun. (ICC)*, May 2016, pp. 1–6.

[16] C.-L. Cheng and A. Zajic, "Characterization of propagation phenomena relevant for 300 GHz wireless data center links," *IEEE Trans. Antennas Propag.*, vol. 68, no. 2, pp. 1074–1087, Feb. 2020.

[17] Y. Xing and T. S. Rappaport, "Propagation measurement system and approach at 140 GHz-moving to 6G and above 100 GHz," in *Proc. IEEE Global Commun. Conf. (GLOBECOM)*, Dec. 2018, pp. 1–6.

[18] K. Guan *et al.*, "Measurement, simulation, and characterization of train-to-infrastructure inside-station channel at the terahertz band," *IEEE Trans. THz Sci. Technol.*, vol. 9, no. 3, pp. 291–306, May 2019.

[19] K. Sato, M. Fujise, R. Tachita, E. Hase, and T. Nose, "Propagation in ROF road-vehicle communication system using millimeter wave," in *Proc. IEEE Int. Vehicle Electron. Conf. (IVEC)*, Sep. 2001, pp. 131–135.

[20] E. Ben-Dor, T. S. Rappaport, Y. Qiao, and S. J. Lauffenburger, "Millimeter-wave 60 GHz outdoor and vehicle AOA propagation measurements using a broadband channel sounder," in *Proc. IEEE Global Telecommun. Conf. (GLOBECOM)*, Dec. 2011, pp. 1–6.

[21] A. Kato, K. Sato, M. Fujise, and S. Kawakami, "Propagation characteristics of 60-GHz millimeter waves for ITS inter-vehicle communications," *IEICE Trans. Commun.*, vols. E84–B, pp. 2530–2539, Sep. 2001.

[22] R. Schneider, D. Didascalou, and W. Wiesbeck, "Impact of road surfaces on millimeter-wave propagation," *IEEE Trans. Veh. Technol.*, vol. 49, no. 4, pp. 1314–1320, Jul. 2000.

[23] V. Petrov, J. Kokkoniemi, D. Moltchanov, J. Lehtomaki, M. Juntti, and Y. Koucheryavy, "The impact of interference from the side lanes on mmWave/THz band V2V communication systems with directional antennas," *IEEE Trans. Veh. Technol.*, vol. 67, no. 6, pp. 5028–5041, Jun. 2018.

[24] V. Petrov, J. M. Eckhardt, D. Moltchanov, Y. Koucheryavy, and T. Kurner, "Measurements of reflection and penetration losses in low terahertz band vehicular communications," in *Proc. 14th Eur. Conf. Antennas Propag. (EuCAP)*, Mar. 2020, pp. 1–5.

[25] K. Hall *et al.*, "Long-life concrete pavements in Europe and Canada," Amer. Trade Initiatives, Alexandria, VA, USA, Tech. Rep. FHWA-PL-07-027, Aug. 2007. [Online]. Available: https://international.fhwa.dot.gov/pubs/pl07027/pl07027.pdf

[26] E. J. Jaselskis, J. Grigas, and A. Brilingas, "Dielectric properties of asphalt pavement," *J. Mater. Civil Eng.*, vol. 15, no. 5, pp. 427–434, Oct. 2003.

[27] S. Rey, J. M. Eckhardt, B. Peng, K. Guan, and T. Kurner, "Channel sounding techniques for applications in THz communications: A first correlation based channel sounder for ultra-wideband dynamic channel measurements at 300 GHz," in *Proc. 9th Int. Congr. Ultra Modern Telecommun. Control Syst. Workshops (ICUMT)*, Nov. 2017, pp. 449–453.

[28] J. Liang, J. Lee, M.-D. Kim, and X. Yin, "Synthesis techniques of narrow beam-width directional antenna measurements for millimeter-wave channel characterization," in *Proc. Int. Conf. Inf. Commun. Technol. Converg. (ICTC)*, Oct. 2015, pp. 689–693.

[29] A. Yamamoto, K. Ogawa, T. Horimatsu, A. Kato, and M. Fujise, "Path-loss prediction models for intervehicle communication at 60 GHz," *IEEE Trans. Veh. Technol.*, vol. 57, no. 1, pp. 65–78, Jan. 2008.
[30] S. Takahashi, A. Kato, K. Sato, and M. Fujise, "Distance dependence of path loss for millimeter wave inter-vehicle communications," in *Proc. IEEE 58th Veh. Technol. Conf. (VTC)*, vol. 1, Oct. 2003, pp. 26–30.
[31] *Study on Channel Model for Frequencies From 0.5 to 100 GHz (Release 14)*, document TR 38.901 V14.3.0, 3GPP, Jan. 2018.
[32] H. Wang, X. Yin, X. Cai, H. Wang, Z. Yu, and J. Lee, "Fading characterization of 73 GHz millimeter-wave V2V channel based on real measurements," in *Proc. Int. Workshop Commun. Technol. Vehicles*. New York, NY, USA: Springer, 2018, pp. 159–168.
[33] I. K. Jain, R. Kumar, and S. S. Panwar, "The impact of mobile blockers on millimeter wave cellular systems," *IEEE J. Sel. Areas Commun.*, vol. 37, no. 4, pp. 854–868, Apr. 2019.
[34] J. Kokkoniemi, J. Lehtomaki, and M. Juntti, "Measurements on penetration loss in terahertz band," in *Proc. 10th Eur. Conf. Antennas Propag. (EuCAP)*, Apr. 2016, pp. 1–5.
[35] M. Boban *et al.*, "Multi-band vehicle-to-vehicle channel characterization in the presence of vehicle blockage," *IEEE Access*, vol. 7, pp. 9724–9735, Jan. 2019.
[36] J.-J. Park, J. Lee, J. Liang, K.-W. Kim, K.-C. Lee, and M.-D. Kim, "Millimeter wave vehicular blockage characteristics based on 28 GHz measurements," in *Proc. IEEE 86th Veh. Technol. Conf. (VTC)*, Sep. 2017, pp. 1–5.
[37] J.-J. Park, J. Lee, K.-W. Kim, K.-C. Lee, and M.-D. Kim, "Vehicle antenna position dependent path loss for millimeter-wave V2V communication," in *Proc. 11th Global Symp. Millim. Waves (GSMM)*, May 2018, pp. 1–3.
[38] W. Fan, F. Zhang, Z. Wang, O. K. Jensen, and G. F. Pedersen, "On angular sampling intervals for reconstructing wideband channel spatial profiles in directional scanning measurements," *IEEE Trans. Veh. Technol.*, vol. 69, no. 11, pp. 13910–13915, Nov. 2020.
[39] T. S. Rappaport, *Wireless Communications: Principles and Practice*, 1st ed. Piscataway, NJ, USA: IEEE Press, 1996.
[40] M. G. Sánchez, M. P. Táboas, and E. L. Cid, "Millimeter wave radio channel characterization for 5G vehicle-to-vehicle communications," *Measurement*, vol. 95, pp. 223–229, Jan. 2017.

Johannes M. Eckhardt was born in Braunschweig, Germany, in 1992. He received the Dipl.Ing. degree in communications and information technology from Technische Universität Dresden, Germany, and the M.A. degree in electrical engineering from the Ecole Centrale Paris, France, in 2017. He is currently pursuing the Ph.D. degree with the Department of Mobile Radio Systems, Institute for Communications Technology, Technische Universität Braunschweig, Germany. His research interests include channel measurements and modeling, link-level simulations, and beam steering in complex scenarios for multi gigabit communication systems at THz frequencies.

Vitaly Petrov (Member, IEEE) received the Specialist degree in information systems security from SUAI University, St. Petersburg, Russia, in 2011, the M.Sc. degree in IT and communications engineering from the Tampere University of Technology, Tampere, Finland, in 2014, and the Ph.D. degree in communications engineering from Tampere University, Tampere, in 2020. He was a Visiting Researcher with The University of Texas at Austin, TX, USA, in 2018, a Visiting Researcher with the University at Buffalo, The State University of New York, NY, USA, in 2016 and 2019, and a Visiting Researcher with the University of Technology Braunschweig, Germany, in 2019. He was also a Visiting Scholar with the Georgia Institute of Technology, Atlanta, GA, USA, in 2014. Since 2020, he has been a Senior Standardization Specialist and a 3GPP RAN1 Delegate with Nokia Bell Labs, Helsinki, Finland. His current research interests include mmWave and THz band communications, softwarized networks, cryptology, and network security. He was a recipient of the Best Student Paper Award at IEEE VTC-Fall 2015, the Best Student Poster Award at IEEE WCNC 2017, and the Best Student Journal Paper Award from IEEE Finland in 2019.

Dmitri Moltchanov received the M.Sc. and Cand.Sc. degrees from the St. Petersburg State University of Telecommunications, Russia, in 2000 and 2003, respectively, and the Ph.D. degree from the Tampere University of Technology in 2006. He is currently a University Lecturer with the Laboratory of Electronics and Communications Engineering, Tampere University, Finland. He has (co)authored more than 150 publications on wireless communications, heterogeneous networking, the IoT applications, and applied queuing theory. In his career, he has taught more than 50 full courses on wireless and wired networking technologies, the P2P/IoT systems, network modeling, and queuing theory. His current research interests include research and development of 5G/5G+ systems, ultrareliable low-latency service, the industrial IoT applications, mission-critical V2V/V2X systems, and blockchain technologies.

Yevgeni Koucheryavy (Senior Member, IEEE) received the Ph.D. degree from the Tampere University of Technology in 2004. He is currently a Professor and the Lab Director of the Unit of Electrical Engineering, Tampere University, Finland. He is the author of numerous publications in the field of advanced wired and wireless networking and communications. His current research interests include various aspects in heterogeneous wireless communication networks and systems, the Internet of Things and its standardization, and nanocommunications. He is an Associate Technical Editor of *IEEE Communications Magazine* and an Editor of the IEEE COMMUNICATIONS SURVEYS AND TUTORIALS.

Thomas Kürner (Fellow, IEEE) received the Dipl.Ing. degree in electrical engineering and the Dr.Ing. degree from the University of Karlsruhe, Germany, in 1990 and 1993, respectively. From 1990 to 1994, he was with the Institut für Höchstfrequenztechnik und Elektronik (IHE), University of Karlsruhe, working on wave propagation modeling, radio channel characterization, and radio network planning. From 1994 to 2003, he was with the Radio Network Planning Department at the Headquarters of the GSM 1800 and UMTS Operator E-Plus Mobilfunk GmbH and Company KG, Düsseldorf, where he was the Team Manager of radio network planning support responsible for radio network planning tools, algorithms, processes, and parameters, from 1999 to 2003. Since 2003, he has been a Full University Professor of mobile radio systems with Technische Universität Braunschweig. In 2012, he was a Guest Lecturer with Dublin City University within the Telecommunications Graduate Initiative in Ireland. He was the Chair of IEEE 802.15.3d TG 100G, which developed the worldwide first wireless communications standard operating at 300 GHz. Since 2016, he has been a member of the Board of Directors of the European Association on Antennas and Propagation (EurAAP). In 2019, he received the Neal-Shephard Award of the IEEE Vehicular Technology Society (VTS). He is also the Chair of the IEEE 802.15 Standing Committee THz. He is also the Project Coordinator of the H2020-EU-Japan Project TeraHertz end-to-end wireless systems supporting ultrahigh data Rate applications (ThoR) and a Coordinator of the German DFG-Research Unit for 2863 Metrology for THz Communications (Meteracom). Since 2020, he has been a Distinguished Lecturer of the IEEE Vehicular Technology Society.